



# Influence of Heat Treatment on the Microstructure and Corrosion Behavior of Thixo-cast Mg-Y-Nd-Zr

Z. Szklarz and Ł. Rogal

(Submitted May 31, 2019; in revised form July 26, 2020; published online September 10, 2020)

The influence of semisolid metal processing (SSM, also called thixoforming) and T6 heat treatment (HT) on the microstructure and corrosion behavior in chlorides of Mg-Y-Nd-Zr (WE43B) magnesium alloy was investigated. The as-cast microstructure is composed of  $\alpha$ -Mg grains with the size of  $52.8 \pm 1.9 \mu\text{m}$  surrounded by eutectic precipitations enriched in rare-earth elements (Y, Nd). The thixo-cast microstructure contained  $\alpha$ -Mg globular grains with the size of  $65.5 \pm 2.1 \mu\text{m}$  surrounded by a fine eutectic mixture in the volume of 26.6%. The T6 HT (heat treatment and saturation at  $525^\circ\text{C}/5 \text{ h}$ , cooling in  $\text{H}_2\text{O}$  and aging at  $190^\circ\text{C}/48 \text{ h}$ ) caused an increase of yield strength to 180 MPa and tensile strength to 280 MPa at the hardness  $105 \pm 4 \text{ HV}_5$ . Next, the electrochemical response was investigated in 0.1 M NaCl using the global and local LSV (linear sweep voltammetry) and EIS (electrochemical impedance spectroscopy) methods. The EIS method suggests the same mechanism for the processes occurring at the electrode/electrolyte interface and shows higher values of the polarization resistances of treated samples after 24-h immersion tests. In particular, better corrosion resistance in chlorides is observed in the alloy after SSM compared to the SSM/HT specimen, which has also been confirmed by the LSV tests performed after 24-h immersion. By using a local technique, a higher susceptibility of the matrix of SSM and SSM/HT samples to pitting corrosion has been revealed.

**Keywords** corrosion behavior, electrochemical impedance spectroscopy, magnesium alloys, micro-capillary, microstructure, thixoforming

## 1. Introduction

Magnesium belongs to the group of active metals with relatively low electrochemical potential ( $E^\circ = -2.4 \text{ V}$  vs. SHE), indicating a very high tendency to undergo oxidation (Ref 1-5). This feature of pure Mg and its alloys results in electrochemical activity, which is the reason for susceptibility to corrosion in highly conductive environments, like water solutions. On the other hand, magnesium alloys are promising as structural materials due to their low weight and environmental friendliness (Ref 6, 7). Nevertheless, their application is still relatively limited because of their low ductility and strength. At present, studies are focused on developing new chemical compositions and their further optimization as well as on new forming technologies (Ref 8, 9). Rokhlin et al. (Ref 10) indicated that the addition of rare-earth elements (RE), such as Gd, Y, Nd and mischmetal, leads to significant improvement in specific strength at both room and elevated temperatures, as well as creep resistance.

There are many types of conventional magnesium-forming technologies (e.g., casting or plastic deformation, like rolling or

extrusion), which bring about an improvement in mechanical properties and, at the same time, a significant impact on corrosion behavior (Ref 11-16). A new alternative to the above-mentioned forming methods is semisolid metal processing (SSM), which utilizes the thixotropic behavior of metal alloys containing 15-80% of liquid fraction. This is possible when the microstructure in the solidus-liquidus range consists of globular grains surrounded by a uniformly distributed liquid (Ref 17, 18). The generation of globular morphology within the alloy microstructure is an essential step in all SSM technologies (Ref 19). Depending on the method employed, a different grain size and a different fraction of the liquid phase are obtained (Ref 17, 20). In the case of Mg alloys, the SIMA (strain-induced melting-activated) (Ref 21-23) and RAP (recrystallization and partial remelting) methods (Ref 24) are most commonly used. Another familiar method is modification, in which the heterogeneous nucleation of solid solution grains is applied (Ref 25).

The alloy composition and the forming technology affect the corrosion behavior (Ref 26-40). The corrosion properties are particularly important when the material can be used as an implant. It is well known that Mg alloys possess a similar Young's modulus to that of human bones; thus, they are promising materials for the elements used in bone surgery. Because magnesium is nontoxic, its alloys can be used as temporary implants, which after some time dissolve without harming the human body (Ref 41-43). In addition, some Mg-RE (rare-earth elements) alloys can be used as biomedical materials (Ref 44-46).

The scientific goal presented in this paper was to analyze how the SSM process (thixo-casting, thixoforming) and the T6 heat treatment influence the microstructure, mechanical properties and corrosion behavior of the WE43 magnesium alloy. This has been carried out due to a lack of knowledge about the possible use of the WE43 alloy as a biomedical material, where

Z. Szklarz, Department of Chemistry and Corrosion of Metals, Faculty of Foundry Engineering, AGH-University of Science and Technology, 23 Reymonta Str., 30-059 Cracow, Poland; and Ł. Rogal, Institute of Metallurgy and Materials Science, Polish Academy of Sciences, 25 Reymonta Str., 30-059 Cracow, Poland. Contact e-mails: zszklarz@agh.edu.pl and l.rogal@imim.pl.

its properties (like mechanical strength and corrosion resistance) after SSM should be explained in more detail.

## 2. Experimental Procedures

### 2.1 Material and Sample Preparation

A magnesium-based alloy with additives (4.2 wt.% Y; 2.5 wt.% Nd; and 0.53 wt.% Zr), which corresponds to the specification for Elektron WE43B (AMS 4427), was used in the present study. The alloy was supplied in the form of as-cast ingots by Magnesium Electron Ltd. The semisolid metal processing (also called thixoforming) of the WE43B magnesium alloy was conducted using a specially built press prototype, as described in previous papers (Ref 19, 47). The ingot was heated up to 625 °C, and the heating rate was about 70 °C/min, which corresponded to about 25% of the liquid phase. The pressing process was executed at the pressing force of 300 kN.

### 2.2 Analysis of Microstructure and Mechanical Properties

A light microscope (Nikon Eclipse L100) was used for the optical observations of the surface of the WE43 magnesium alloy and also in combination with the electrochemical microcell technique to investigate local corrosion behavior. The microstructure was also examined by applying an FEI SEM XL30 scanning electron microscope (SEM) working in back-scattered electron (BSE) or secondary electron (SE) modes. The chemical composition of selected microareas was established using the energy-dispersive x-ray spectroscopy (EDS) technique with an EDAX Apollo XP spectrometer. Five measurements were made for each phase, and the mean value and standard deviation were calculated. The phase analysis was carried out with a Philips PW 1710 diffractometer and Co K $\alpha$  filtered radiation in the scan mode in the range 20–100 of 2-Theta at the anode voltage of 40 kV and current of 40 mA. The PDF-4+ cryptographic database (the International Center for Diffraction Data), Panalytical Data Viewer, High Score Plus and Match programs were used to identify the phases. The tensile strength test was performed using an INSTRON 3382 machine in accordance with the PN-EN ISO 6892-1:2016-09 standard. The Vickers hardness was measured using a Zwick/ZHU 250 tester under the load of 5 kg in accordance with ASTM E92.

### 2.3 Electrochemical Measurement Methodology

Corrosion behavior studies were performed by using a classical electrochemical three-electrode system (Ref 48, 49). The tested specimens acted as working electrodes with 0.5 cm<sup>2</sup> of exposed surface, with the reference electrode being Ag/AgCl (containing 3 M KCl electrolyte) and a platinum plate working as a counter electrode. All electrochemical tests were conducted in a 0.1 M NaCl water solution and at room temperature (about 20 °C).

To investigate the corrosion behavior of the samples on the global scale, three basic electrochemical methods were employed: first, the open circuit potential measurement (OCP) during 24 h of the specimen immersion, second, linear sweep voltammetry (LSV) with the sweep rate of 1 mV s<sup>-1</sup> and with the beginning potential from -2 V vs. Ag/AgCl toward anodic

potential, and third, the electrochemical impedance spectroscopy (EIS) at OCP (with a sinusoidal perturbation signal of 10 mV amplitude and a 10 kHz to 5 mHz frequency range).

The above-mentioned electrochemical microcell technique (EMT) was also employed to investigate the local corrosion behavior (Ref 50–54). EMT allows electrochemical measurements to be performed on the microscale and local corrosion behavior to be characterized. This technique consists of a glass microcapillary that is filled with an electrolyte (Fig. 1a). The microcapillary tip was sealed to the specimen surface with a layer of silicon rubber. The microcell (connected with the capillary) was mounted on a microscope for precise positioning of the microcapillary on the surface (Fig. 1b). The size of the microcapillary tip used during studies of the WE43 magnesium alloy was about 50  $\mu$ m in diameter. The counter electrode was a platinum wire, and the reference electrode was Ag/AgCl (3 M KCl). The LSV electrochemical method was used during local studies.

## 3. Results and Discussion

### 3.1 Microstructure and Mechanical Properties

The analysis based on scanning electron microscopy of as-cast WE43B (ingot) is presented in Fig. 2(a) and (b). The grains of  $\alpha$ -Mg surrounded by the eutectic can be seen giving a light-gray diffusive contrast and a strong bright contrast (3.1 vol. %) coming from the phases which solidified as the last ones. The circularity index of solid solution grains was  $0.72 \pm 0.1$ , and the average size was  $52.8 \pm 1.9 \mu$ m. The chemical composition from the middle part of the grains (point 1, Table 1, Fig. 2a) confirmed the presence of a predominant amount of magnesium at a small amount of RE. The grain areas with the gray diffusive contrast occupied 19.3 vol. % of the image surface, while the concentration of RE elements was significantly higher (point 2, Fig. 2(a), Table 1), suggesting the segregation of RE-rich phases at grain boundaries and the formation of the eutectic (morphology typical for this phase). The EDS analysis from the area where white contrast is present (points 3–5 in Fig. 2(b), Table 1) confirmed the high content of Y and Nd, suggesting the eutectic contains phases enriched in RE elements.

The addition of RE elements, such as Gd and Nd, has a significant impact on the microstructure, which leads to grain refinement by the heterogeneous nucleation of  $\alpha$ -Mg. The Zr addition also results in the formation of Zr-rich particles that are nuclei during solidification, which leads to grain refining. ZnZr<sub>2</sub> precipitations on the grain boundaries limit the microstructure coarsening (Ref 55, 56).

According to the binary diagrams developed by Massalski (Ref 57), it could be deduced that for Mg-Nd, Mg-Gd and Mg-Y systems, the solubility of neodymium, gadolinium and yttrium in magnesium is about 4.2 wt.% at the temperature of 535 °C, 3.75 wt.% at 566 °C and 11.4 wt.% at 567 °C, respectively. This proves that the metals have limited solubility in the solid state, and the T6 heat treatment is required to dissolve the RE in the Mg matrix in order to improve their properties by precipitation hardening and solution hardening. The Zr-enriched precipitations were present around the grain area, leading to the limitation of its coarsening (Ref 58). The x-ray analysis (Fig. 3a) confirmed the presence of a predominant

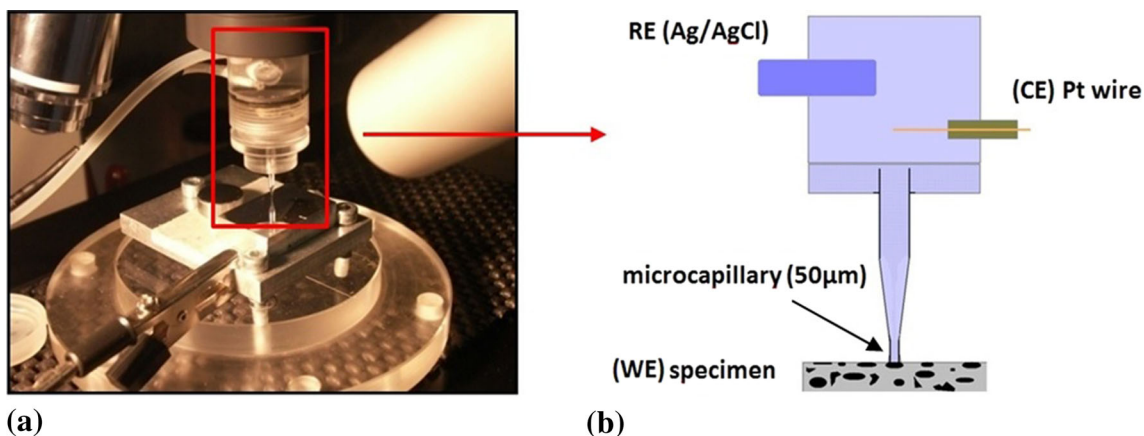


**Fig. 1** (a) Experimental setup of the electrochemical microcell technique (EMT) used for these experiments, (b) a sketch presenting the principle of EMT usage

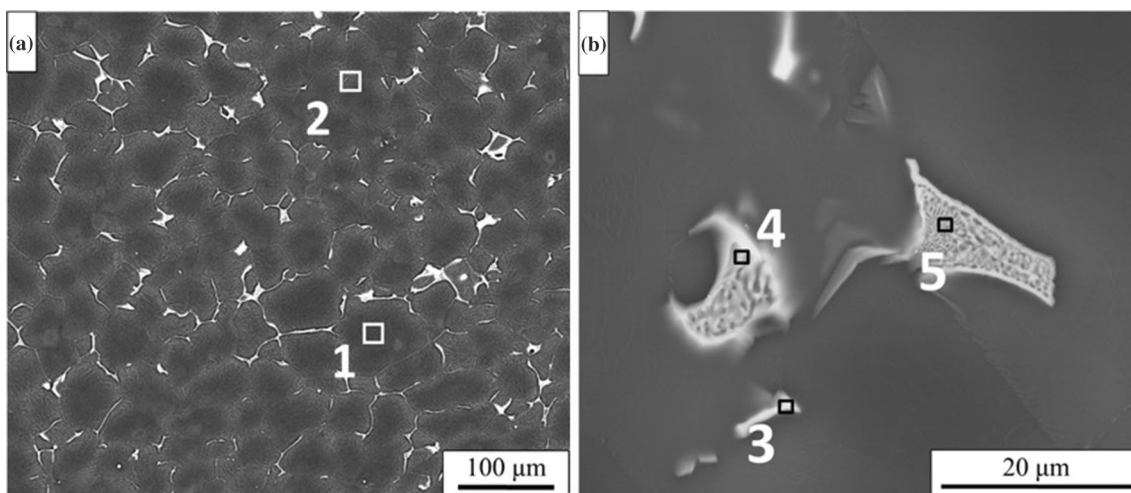


**Fig. 2** SEM-BSE images of the as-cast WE43B: (a) overall view of sample microstructure, (b) high magnification of interglobular area with marked points of EDS analysis

**Table 1** Chemical composition of phases in the as-cast WE43B measured with SEM/EDS and TEM/EDS techniques [areas marked in Fig. 2(a) and (b), 5(b) and 6(b)]

Place of analysis		Content, wt.%/at.%			
		Mg	Y	Zr	Nd
Figure 2(a) and (b)	1	98.6/99.7	0.4/0.1	0.2/0.1	0.8/0.1
	2	95.2/ 98.8	3/ 0.8	0/0	1.6/ 0.3
	3	74.65/ 93.4	9.5/ 3.2	0.1/ 0.1	15.8/3.3
	4	70.45/ 92.05	10.5/3.75	0/0	19.1/4.2
	5	73.05/ 93.07	8.51/ 2.97	0/0	18.44/ 3.96
Figure 5(b)	1	95.6/ 99.3	1.6/ 0.4	0.3/ 0.1	1.1/ 0.1
	2	91.1/ 97.8	5.3/ 1.6	...	3.6/ 0.6
	3	69.0/ 91.7	11.9/ 4.3	...	18.2/ 4.2
	4	65.1/ 90.1	14.6/ 5.4	0.3/ 0.1	19.0/ 4.4
Figure 6(b)	1	92.3/ 98.1	4.6/ 1.3	...	2.8/ 0.5
	2	60.9/ 88.6	11.5/ 4.7	0.3/ 0.1	27.2/ 6.7

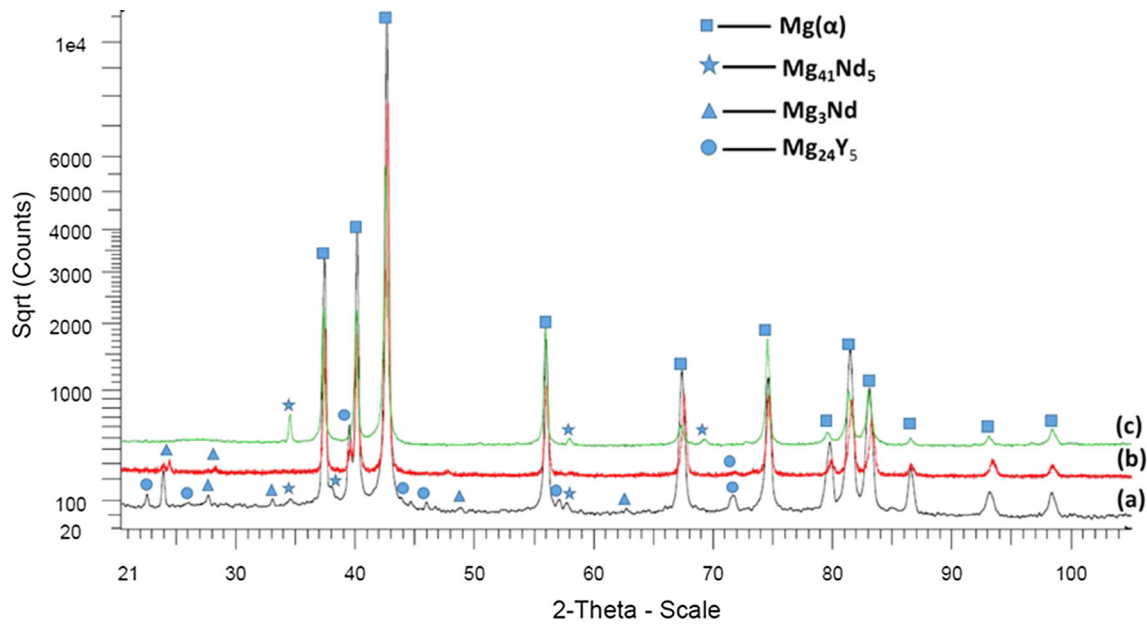


**Fig. 3** X-ray diffractograms of the WE43B magnesium alloy: (a) as-cast, (b) thixo-cast, (c) thixo-cast after the T6 heat treatment

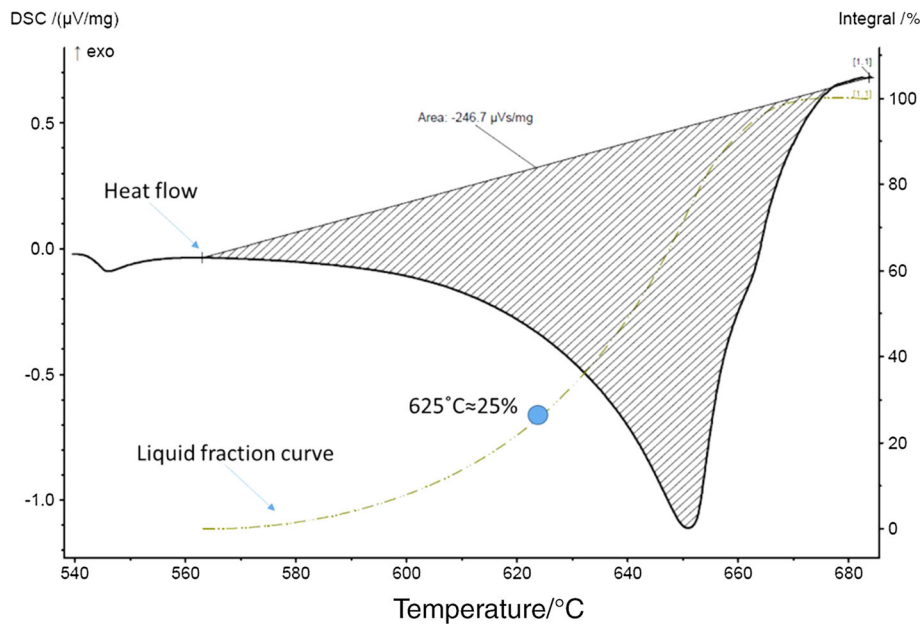


**Fig. 4** DSC heating flow run and the liquid fraction curve for a WE43B ingot

amount of  $\alpha$ -Mg in small concentrations of  $\text{Mg}_{24}\text{Y}_5$ ,  $\text{Mg}_{41}\text{Nd}_5$  and  $\text{Mg}_3\text{Nd}$  intermetallic phases located inside the eutectic areas, which are at the grain boundaries.

The WE43B magnesium alloy ingot was used as a feedstock for semisolid processing to assess the influence of technology on the microstructure, mechanical and corrosion properties. As confirmed in several works (Ref 59, 60), SSM allows a unique structure to be obtained, thanks to the specific conditions of the process, for example, high shearing during the flow of the alloy suspension, rapid cooling, exerted pressure during the solidification and, consequently, the formation of a strong nonequilibrium state of material.

In Fig. 4, the DSC curve (solid line) shows the endothermic effects which occurred during heating at the rate of 20 K/min. Additionally, the dashed double-dotted curve in Fig. 4 shows the dependence of the calculated amount of the liquid phase as a function of temperature. The melting point is determined as the onset of the endothermic peak. The start of melting is set at such a temperature when the heat curve falls away from the tangent line. The end of melting is set by the onset point on the other side of the peak. The enthalpy of the melting process is  $-246.7 \mu\text{Vs/mg}$ . The semisolid processing was carried out at  $625^\circ\text{C}$ , which corresponds to 25% of the liquid phase in accordance with the DSC analysis (the point marked in Fig. 4).



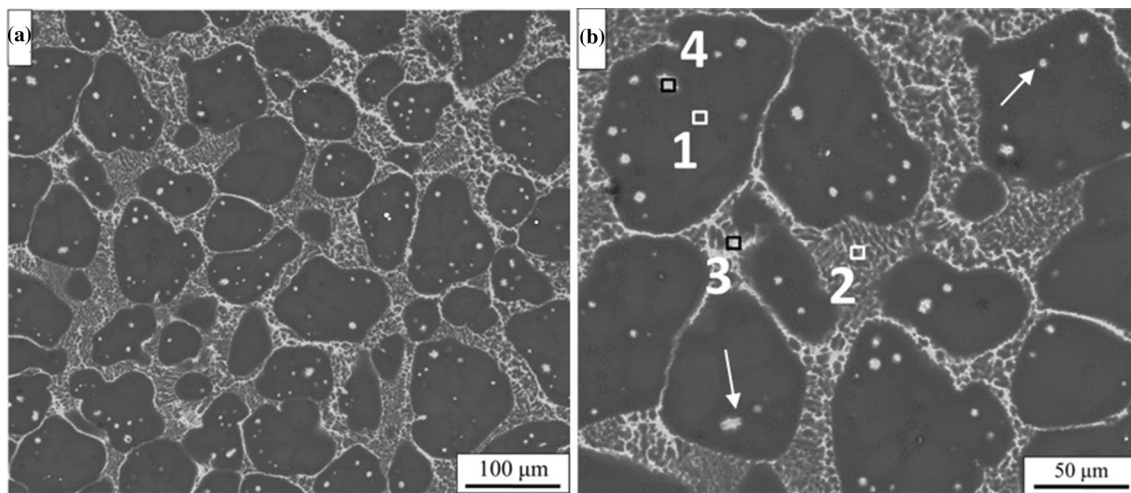


**Fig. 5** SEM-BSE images of the thixo-cast WE43B: (a) globular grains with the eutectic mixture, (b) magnified area with marked points of EDS analysis

The SEM-BSE microstructure of the thixo-cast WE43B revealed the presence of  $\alpha$ -Mg globular grains with an average size of  $65.5 \pm 2.1 \mu\text{m}$ , surrounded by the eutectic mixture and secondary solid solution (Fig. 5a). Based on image analysis, the liquid fraction in a semisolid range (area around grains) was in the volume of 25.5%. The XRD analysis confirmed the presence of  $\alpha$ -Mg and  $\text{Mg}_{24}\text{Y}_5$ ,  $\text{Mg}_3\text{Nd}$ , at lower content, in comparison with the ingot structure of  $\text{Mg}_{41}\text{Nd}_5$  which partially dissolved in the magnesium matrix (Fig. 3b). The results of EDS point analysis in the grain (point 1 in Fig. 5b) as well as in the eutectic (points 2 and 3 in Fig. 5b) are presented in Table 1. Significant microstructure changes in comparison with the WE43B ingot are visible. This is connected with the sample remaining in the semisolid state, which leads to diffusion control phenomena, such as an increase in average grain sizes as well as increases in the concentration of RE elements in the grains (point 1 Fig. 2(a) and (b) and point 1 Fig. 5(a), Table 1). This suggests that, after SSM, alloy grains are partially saturated while the eutectic is refined through rapid cooling to a steel die. Additionally, small bright areas inside grains in the volume of 1.1% are visible. The EDS analysis (point 4, Fig. 5, Table 1) confirmed the increased concentration of RE elements. According to references (Ref 24, 61), these are micro-eutectics, which formed inside the grains due to segregation phenomena. These regions of micro-eutectics decrease the effective liquid fraction present between globules, thus negatively affecting the alloy flow behavior during semisolid processing.

The T6 heat treatment of thixo-cast samples was performed in the next stage of the study. The saturation temperature, aging and time of processes were determined based on DSC results (not presented here) and our previous studies (Ref 47). The SEM microstructures after saturation at  $525^\circ\text{C}/5 \text{ h}$  and cooling in  $\text{H}_2\text{O}$  and aging at  $190^\circ\text{C}/48 \text{ h}$  are presented in Fig. 6(a) and (b). Because of the high diffusion of elements at  $525^\circ\text{C}$ , intermetallic phases almost completely dissolved into the magnesium solid solution (resulting in the decrease in its volume) with simultaneous coarsening of the  $\alpha$ -Mg solid solution. Additionally, the SEM-EDS image with the EDS analysis revealed the chemical composition of  $\alpha$ -Mg (point 1 in Fig. 6b, Table 1) and the eutectic in the form of bright

precipitations (point 2 in Fig. 6b, Table 1). From the comparison with the ingot as well as thixo-cast chemistry, it could be seen that  $\alpha$ -Mg was enriched in RE elements. The x-ray analysis also confirmed nearly complete dissolution of  $\text{Mg}_3\text{Nd}$  intermetallic phases after T6 (Fig. 3c), which was visible by the lack of peak intensities (minimum detection is about 3 vol.%) in comparison with the precursors or the thixoformed sample. However, small peaks coming from  $\text{Mg}_{41}\text{Nd}_5$  as well as  $\text{Mg}_{24}\text{Y}_5$  are visible. Aging for 120 h at  $190^\circ\text{C}$  resulted in hardening of the alloy. It is generally accepted that for the Mg-RE alloys aged isothermally at  $120$ – $260^\circ\text{C}$ , the strengthening phases appeared due to the presence of Y and Nd, which are mainly responsible for the precipitation of the metastable  $\beta'$  phases on the prismatic planes of the  $\alpha$ -Mg matrix (Ref 10, 62–64). This was also confirmed by the increase in mechanical properties presented in the next paragraph.

### 3.2 Mechanical Properties

The tensile strength tests were carried out to determine the deformation behavior of the WE43B magnesium alloy after various methods of processing. The stress-strain plots of the ingot (dashed dotted curve; feedstock for SSM), directly after thixoforming (continuous curve) and after T6 (dashed curve), are presented in Fig. 7. The ingot had the lowest tensile strength of 153 MPa at the hardness  $54 \pm 3 \text{ HV}$  and plasticity 12.5%. This was connected with the presence of the coarse eutectic and intermetallic components, and with the lack of nanoprecipitates in the  $\alpha$ -Mg matrix. The thixo-cast WE43B revealed the plastic strain of 6% and the tensile strength of 186 MPa at the yield strength of 110 MPa. The hardness was  $67 \pm 3 \text{ HV}$ . Relatively better mechanical properties are the results of refining the eutectic by rapid quenching to a steel die. The sample contained 26.6% of liquid fraction during the SSM. Due to the fragmentation of the eutectic phase, the strengthening of the interglobular space was higher than that of the input material (ingot). Better properties were achieved during the tensile strength analysis of the samples after heat treatment (saturation from  $525^\circ\text{C}/5 \text{ h}/\text{H}_2\text{O}$  and aging at  $190^\circ\text{C}/48 \text{ h}$ ). Hardness was  $105 \pm 4 \text{ HV}$ . The yield strength of samples after T6 reached 180 MPa, at the tensile strength of 280 MPa. The increase in properties is connected with the formation of

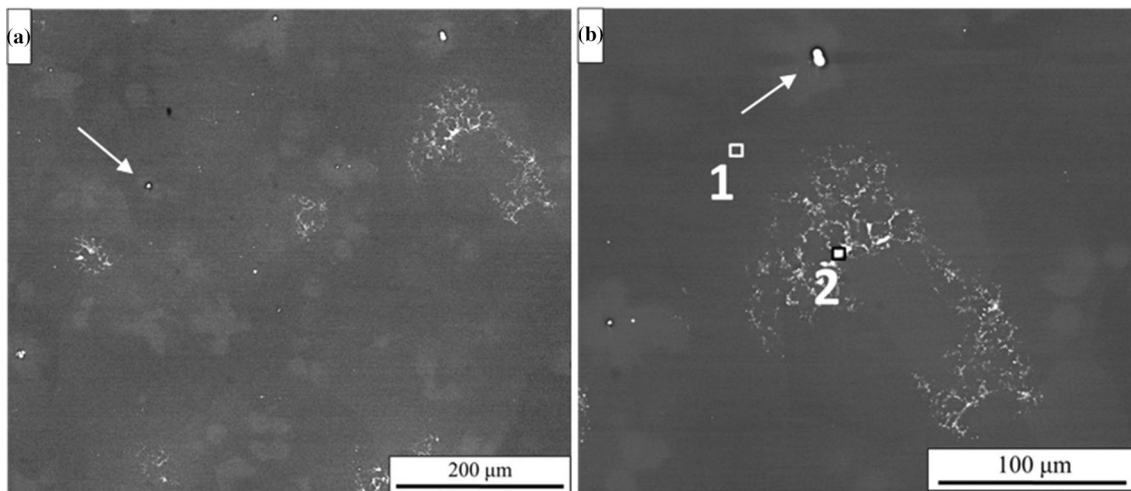


**Fig. 6** SEM-BSE microstructure of the thixo-cast WE43B after the T6 heat treatment: (a) image taken from a large sample area, (b) SEM-BSE image with an area of undissolved eutectic with marked points of EDS analysis

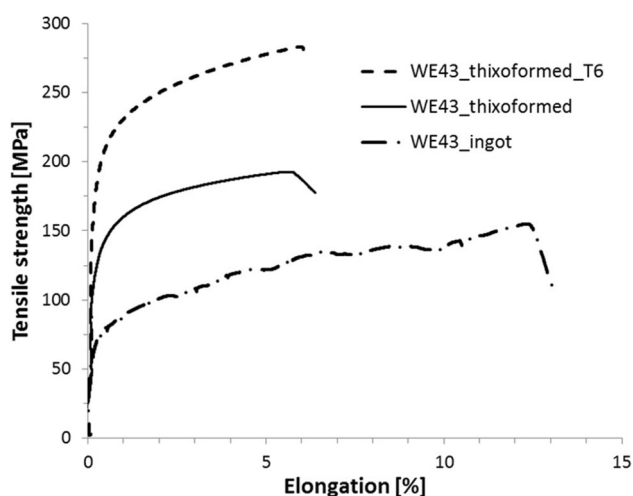


**Fig. 7** Tensile strength curves of WE43B: ingot (dotted dashed curve), directly after thixoforming (continuous curve), after T6: (dashed curve)

nanoprecipitations responsible for strengthening. The increase in the YS value in the thixo-cast after T6 (at 35%) could be connected with an increased number of  $\beta'$  precipitates (due to the application of the solution treatment).

### 3.3 Corrosion Behavior

**3.3.1 The Influence of SSM and T6 Heat Treatment on the Electrochemical Response.** In order to verify the influence of the SSM processing and T6 heat treatment on the electrochemical behavior of the WE43B magnesium alloy, the linear sweep voltammetry (LSV) was recorded after 24-h immersion of samples in the 0.1 M NaCl–water solution (Fig. 8). The electrochemical impedance spectroscopy (EIS) measurements (Nyquist and Bode plots are presented in Fig. 9(a), b and c for the specimen as-cast, thixo-cast (SSM) and thixo-cast after the T6 heat treatment (SSM/HT), respectively) were obtained during immersion for 1, 3, 6 and 24 h in order to verify the course of the corrosion processes on the

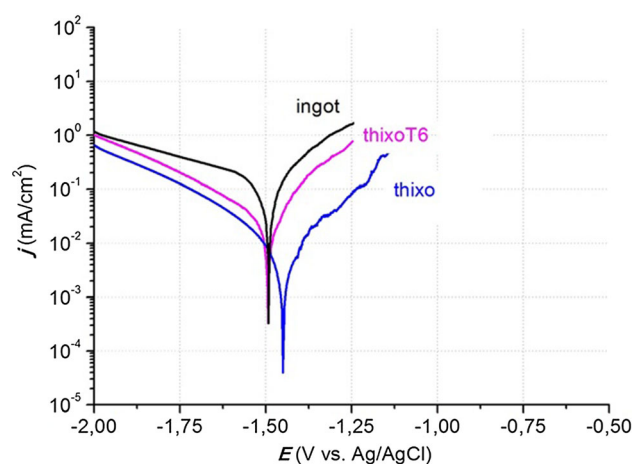


**Fig. 8** LSV obtained after 24-h immersion test (scan rate:  $1 \text{ mV cm}^{-1}$ )

surface of the tested samples. These measurements were made using a sinusoidal signal with the amplitude of 10 mV in the range of frequencies from 10 kHz to 5 mHz. The scattered plots are the measurement results, and solid lines show the calculations, the results of which are collected in Table 3.

In Fig. 8, global potentiodynamic polarization curves (with a  $1 \text{ mV/s}$  scan rate) recorded after 24-h immersion for the tested specimens in the 0.1 M NaCl solution are presented. The electrochemical parameters ( $E_{\text{corr}}$  and  $I_{\text{corr}}$ ) are presented in Table 2. These results show that all three specimens undergo corrosion; nevertheless, the thixo-casting has a strong positive effect and slows down the corrosion rate of the WE43 magnesium alloy. The current density values are much lower for the specimens after SSM and SSM/HT ( $0.012 \text{ mA/cm}^2$  and  $0.032 \text{ mA/cm}^2$ , respectively) compared to the initial state (ingot has  $0.145 \text{ mA/cm}^2$ ), which indicates significant improvement in the corrosion behavior. However, the T6 HT slightly worsens corrosion parameters contrary to the thixo-cast specimen. This will be discussed in the next paragraphs.

As can be seen in Fig. 9(a), (b) and (c), the EIS diagrams are composed of two time constants in the first period of

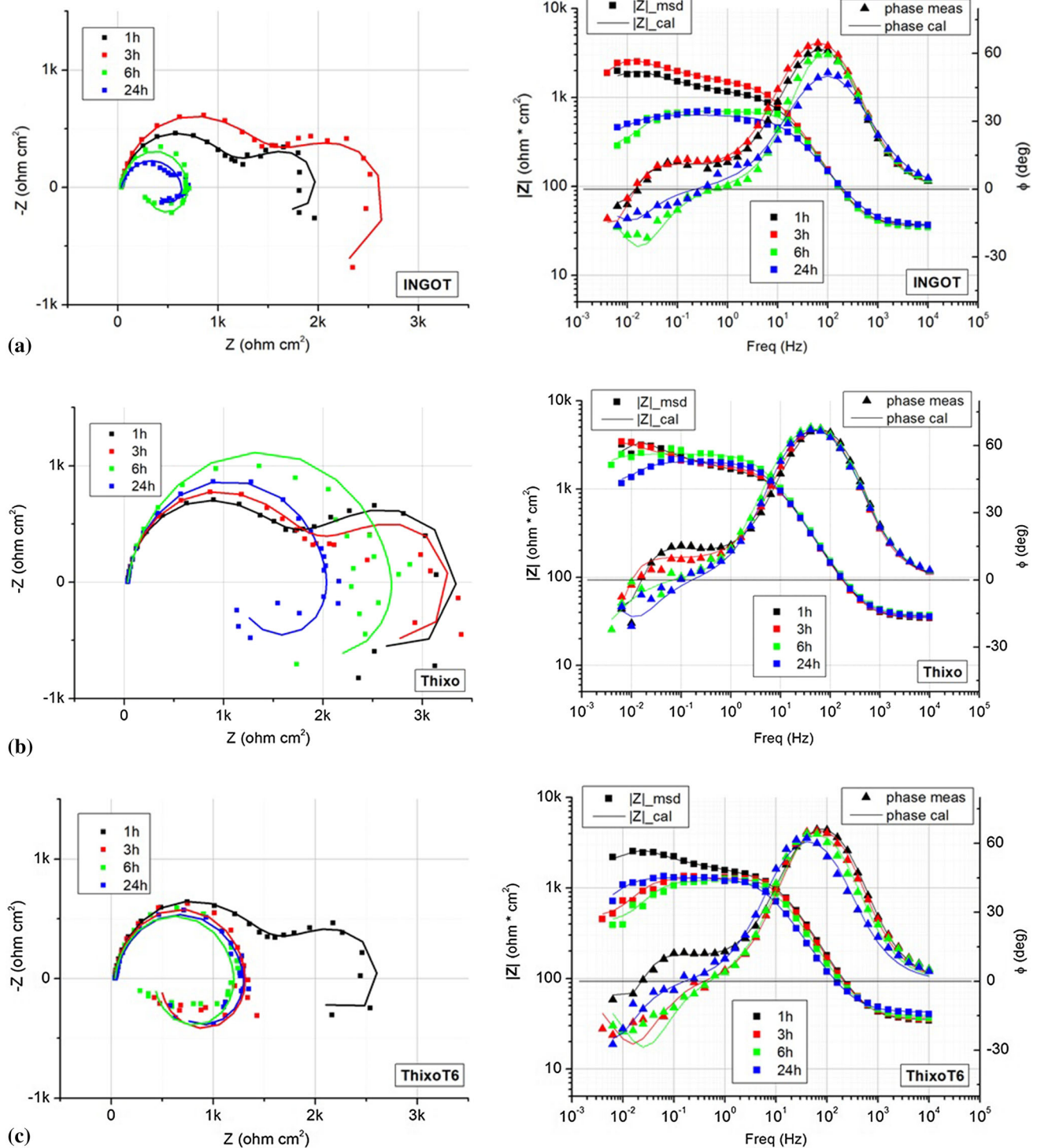


**Fig. 9** Electrochemical impedance spectroscopy (EIS) plots (Nyquist on the left and Bode on the right) obtained during the 24-hour immersion test for: (a) as-cast (ingot) specimen, (b) thixo-cast, (c) thixo-cast after T6 heat treatment

immersion. Next, the electrochemical behavior changes and one time constant remain. Impedance plots have been fitted using the equivalent circuits A (for two time constants) and B (for one time constant) visible in Fig. 10. The numerical data from the EIS simulations are included in Table 3. Fitting the impedance diagrams allows the determination of the electrolyte resistance ( $R_{el}$ ), polarization resistance/charge transfer resis-

tance ( $R_1$ ), which is a measure of the corrosion rate (resistance of the oxide layer or corrosion products which cover the surface of the specimen), constant phase element properties (CPE1) associated with the double layer (in the case of the present investigations, the  $C$  capacitance was replaced with the element  $CPE = 1/Y_0(j\omega)^p$ , which improved the simulation of the impedance spectrums), constant phase element (CPE2), asso-



**Table 2 Electrochemical parameters obtained from polarization curves (Fig. 8)**

Specimen	$E_{\text{corr}}$ (V vs. Ag/AgCl)	$I_{\text{corr}}$ , mA/cm <sup>2</sup>
ingot	− 1.49	0.145
thixo	− 1.45	0.012
thixo-T6	− 1.49	0.032

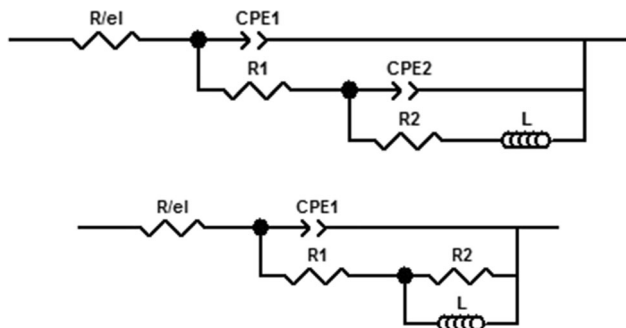


**Fig. 10** Equivalent circuits used for fitting the EIS spectra

ciated with diffusion processes, resistance (R2) and induction values ( $L$ ) related to the corrosion products adsorbed on the surface during corrosion processes.

In the first period of immersion, the EIS response shows two time constants (capacitive loops), where the first peak observed in the Bode diagram (at high frequencies range) is related to the charge transfer resistance which can be used to determine the corrosion rate (Ref 65-67). The second time constant is visible in the lower frequency range, indicating slow processes (like the diffusion of  $\text{Mg}^{2+}$  ions through the porous corrosion product layer) occurring at the electrode/electrolyte interface. The second time constant is present until the corrosion processes (substrate dissolving) have started preceded by dissolution of the layer of corrosion products. This disappears after 3 h of immersion for both the as-cast and thixo-cast specimens and after 1 h of immersion for the thixo-cast/T6 specimen. An inductive loop in EIS diagrams is observed in the lowest frequency range, indicating the adsorption of the corrosion products induced by pitting and dissolution processes (breakdown/dissolution of the corrosion products layer) (Ref 68).

As can be seen in Table 3, the EIS calculations revealed that for the ingot sample the resistance R1 reached  $355 \Omega \text{ cm}^2$  after 24-h immersion. The SSM process (before heat treatment), which modifies the structure of the WE43B alloy and improves the mechanical properties, means that its corrosion resistance also increases. The R1 value for the thixo-cast sample increased up to  $1101 \Omega \text{ cm}^2$ . After the same time of immersion, the corrosion resistance was lower for the thixo-T6 alloy and reached  $586 \Omega \text{ cm}^2$ . Moreover, the drop of the R1 value was observed earlier (after 1 h) than for the ingot and thixo-cast specimens. This indicates a shorter time of immunity of the thixo-T6 specimen in chlorides.

There are also variations in the CPE1 value observed for tested samples during the 24-hour electrochemical test. In the first period of immersion, CPE1 does not change significantly. However, in the case of the ingot specimen, a slight decrease in the CPE1 value during the first 6 h is seen, which can be related

**Table 3 Numerical data derived from the fitting procedure of EIS results**

Specimen: Time:	Ingot				Thixo-cast				Thixo-cast + T6			
	1 h	3 h	6 h	24 h	1 h	3 h	6 h	24 h	1 h	3 h	6 h	24 h
$R_{\text{el}}$ , $\Omega \text{ cm}^2$	37	36	35	35	35	35	36	35	35	36	38	39
$\text{CPE1}$ , $\Omega^{-1} \text{ cm}^{-2} \text{ s}^{\phi}$	$1.8\text{e} - 5$	$1.7\text{e} - 5$	$1.5\text{e} - 5$	$3.6\text{e} - 5$	$1.6\text{e} - 5$	$1.8\text{e} - 5$	$2.1\text{e} - 5$	$2.1\text{e} - 5$	$1.4\text{e} - 5$	$1.5\text{e} - 5$	$1.8\text{e} - 5$	$2.9\text{e} - 5$
$\phi$ -CPE1	0.925	0.926	0.951	0.823	0.940	0.930	0.899	0.906	0.934	0.936	0.927	0.894
R1, $\Omega \text{ cm}^2$	875	1117	242	355	1320	1550	1159	1101	1248	506	485	586
$\text{CPE2}$ , $\Omega^{-1} \text{ cm}^{-2} \text{ s}^{\phi}$	$1.8\text{e} - 3$	$1.3\text{e} - 3$	—	—	$1.1\text{e} - 3$	$1.5\text{e} - 3$	—	—	$1.3\text{e} - 3$	—	—	—
$\phi$ -CPE2	0.296	0.276	—	—	0.350	0.346	—	—	0.327	—	—	—
R2, $\Omega \text{ cm}^2$	883	539	420	248	1014	990	1327	916	889	768	787	774
L, Hcm <sup>2</sup>	23750	36810	2404	2716	34410	50870	66590	8980	16600	3990	2817	12820



to a thick corrosion product film forming on the surface. After 24 h, there is a growth in the CPE1 value for the as-cast specimen which reaches  $3.6 \times 10^{-5} (\Omega^{-1} \text{ cm}^{-2} \text{ s}^{\phi})$ , which is the highest value for the tested specimens. The highest CPE1 values indicate that the corrosion product film and the substrate are strongly dissolved. After 24-h immersion, the lowest value of CPE1 was registered for the thixo-cast and it suggests that there are fewer corrosion products which may be dissolved. This is related to the previously discussed chemical composition of the matrix and precipitations of the network of the second phase (eutectic), which is wide and causes the separation of grains. The wide eutectic network and matrix enriched in RE are the reasons that the specimen is less electrochemically active; thus, it is less covered by corrosion products.

The exponent  $\text{CPE1}-\phi$  values are close to 1 and suggest capacitive properties of the oxide layer on all three samples. After 24 h, the  $\text{CPE1}-\phi$  values become slightly lower for all specimens, which is related to the formation of a thicker layer of corrosion products. This suggests that the character is gently changing from capacitance to diffusion. The highest values of CPE2 for the as-cast specimen suggest the thickest MgO layer and/or its surface area is widely distributed. Moreover, the exponent  $\text{CPE2}-\phi$  values are between 0 and 0.5, which suggests its resistance/diffusive character. It is well known that MgO exhibits semiconductive properties.

**3.3.2 Mechanism of Corrosion in the WE43 Alloy After SSM and SSM/T6 Heat Treatment.** The optical images of cross sections are shown in Fig. 11 together with corroded parts of the surfaces of tested samples after 24-h immersion in the electrolyte. Deep damage can be observed in the matrix of the as-cast specimen after 24-h immersion. The precipitates seem to be untouched, and the dissolution processes bypass them. This is a well-known effect in nonferrous metallic alloys, where precipitates act as local cathodes and there are cathodic reactions on the surface, while the surrounding matrix is dissolving (Ref 69). Moreover, the second-phase precipitations are resistant to chlorides as can be observed, for example, in the case of the AZ91 magnesium alloy; thus, they do not undergo dissolving (Ref 39, 70).

The thixo-cast sample is presented analogically in Fig. 11(b). Because of the presence of the eutectic, which covers a relatively large area on this specimen and appears as a continuous network, the corrosion penetration is not so deep as in the previous case. It can be concluded that large eutectic precipitations inhibit the progress of dissolution. A similar effect was observed in the AZ91 magnesium alloy (Ref 33).

The T6 heat treatment led to microstructural changes, which affected the corrosion behavior. It is visible in Fig. 11(c) that the surface of the thixo-cast/T6 specimen is also “ragged” after 24-h immersion in the electrolyte. The above-mentioned electrochemical measurements revealed a slightly detrimental effect of T6 HT on the corrosion rate. A dual influence of the

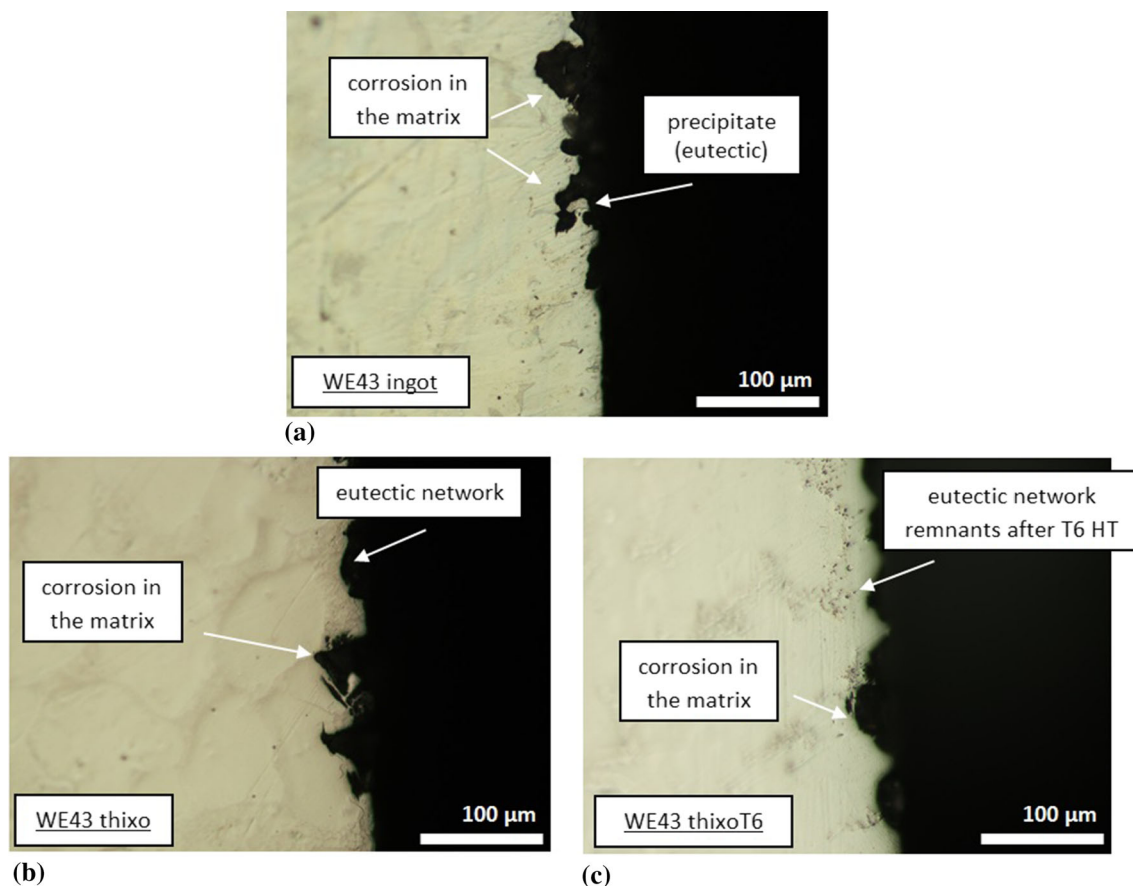


**Fig. 11** Cross-section optical images of the surface (corroded areas) after 24-hour immersion in the electrolyte: (a) ingot specimen, (b) thixo-cast, (c) thixo-cast after heat treatment

microstructure can be observed. First, it is related to the chemical composition of the matrix, which is enriched in RE elements (Fig. 6, Table 1). This means that the dissolution of the matrix is more shallow than in the previous cases. Moreover, the eutectic mixture remnants are much smaller and finer after HT, which leads to a more homogeneous surface

of the thixo-cast/T6 specimen. On the other hand, the discontinuous second-phase precipitations (eutectic remnants) promote the corrosion processes in magnesium alloys.

The SEM images (1000× magnification) together with the EDS analysis results (Table 4) are shown in Fig. 12 for all three tested specimens after 24-h immersion in the electrolyte. It can

**Table 4** EDS analysis results obtained in sites indicated in Fig. 12

Specimen: Site (at.%)	Ingot			Thixo-cast			Thixo-cast + T6		
	+1	+2	+3	+1	+2	+3	+1	+2	+3
O	32.4	31.5	30.3	24.2	24.9	30.1	32.1	32.4	35.7
Mg	66.3	66.9	60.2	74.3	73.3	66.2	64.3	65.3	60.3
Nd	0.16	0.16	4.5	0.14	0.15	0.85	0.37	0.37	1.34
Y	0.68	0.72	4.33	0.70	0.73	1.9	1.21	1.21	2.3
Zr	0.03	0.07	0.17	0.17	0.24	0.12	0.17	0.25	0.13
Cl	0.45	0.52	0.34	0.59	0.56	0.3	0.28	0.37	0.16

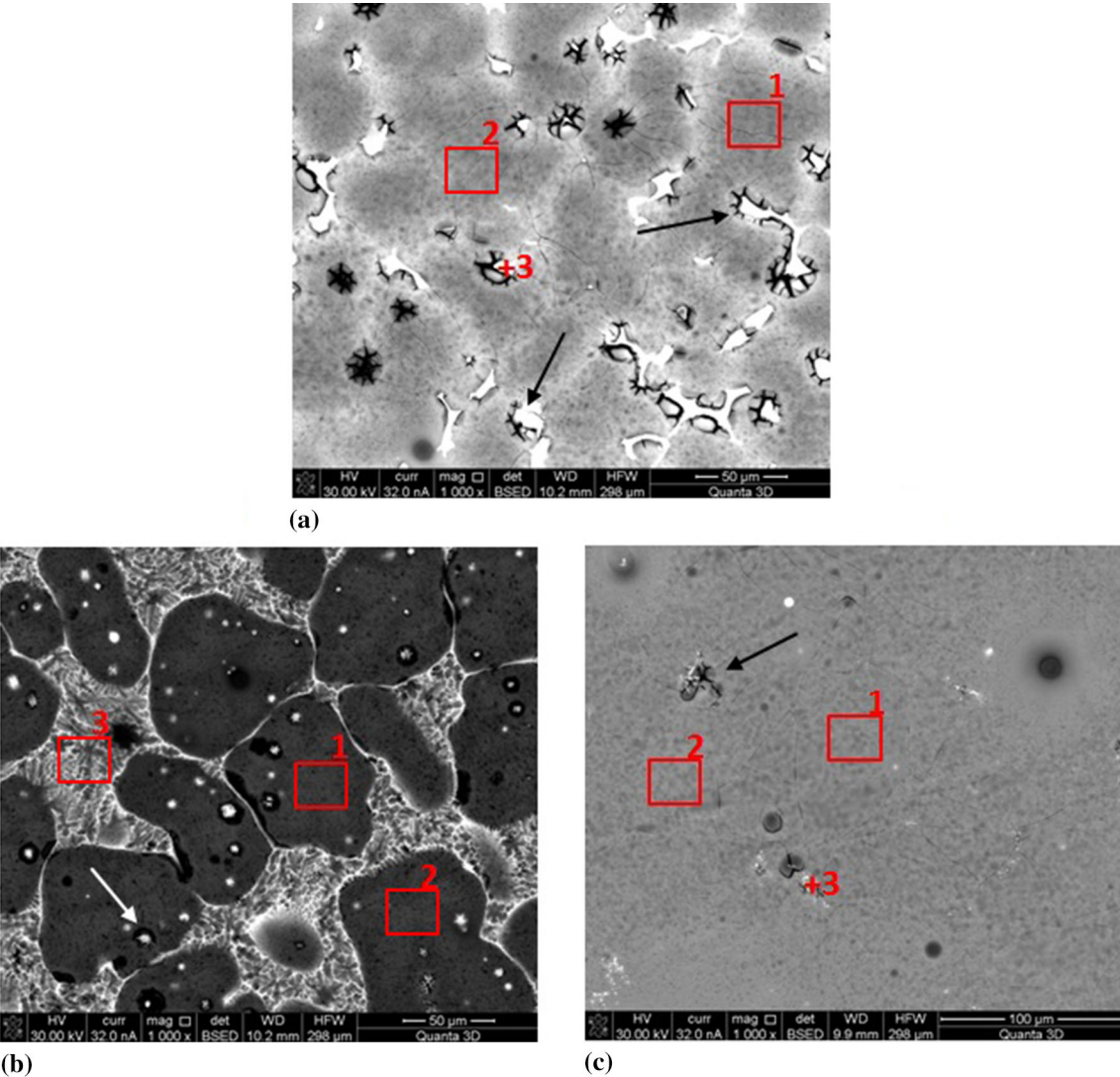


**Fig. 12** SEM images of the surface after 24-h immersion in the electrolyte: (a) ingot specimen, (b) thixo-cast, (c) thixo-cast after heat treatment. Insert: Arrows indicate sites where pitting and/or matrix dissolution occurs (areas surrounding precipitates or inclusions)

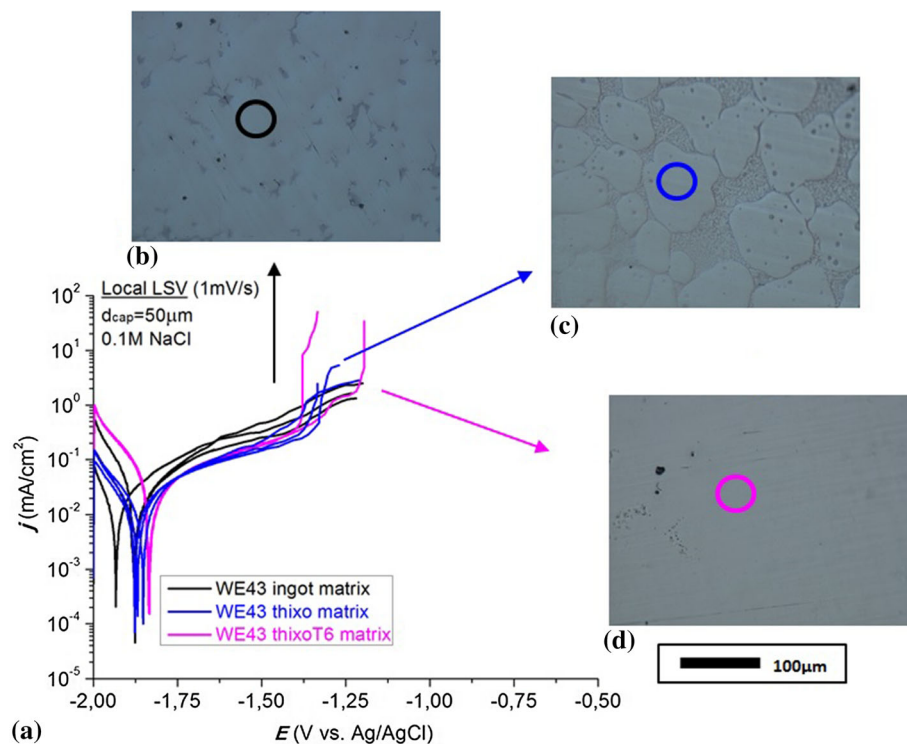


**Fig. 13** (a) Local polarization curves obtained on the matrix of three tested specimens and optical images showing the measurement locations on: (b) the ingot, (c) thixo-cast, (d) thixo-T6 specimens

be seen that significantly higher amounts of oxygen have been registered for all three tested specimens. This is related to the oxidation of the alloy surface, which has been explained above. It should be noted that the lowest value of oxygen has been registered for the thixo-cast specimen.

As the intermetallic phases present in the alloy are enriched in RE (SEM analysis; Fig. 2, 5, 6 and 12), they exhibit a strong cathodic character relative to the matrix (which is anodic). This corrosion mechanism (galvanic corrosion) is very well known and occurs on many ferrous and nonferrous metallic alloys in high-conductivity environments (for example, NaCl water solution). The electrochemical response strongly depends on the chemical composition, size and distribution of the precipitates of intermetallic phases. Thus, the black areas surrounding the precipitates (visible in SEM images after corrosion tests, Fig. 12) confirm the presence of crevices at the matrix/precipitate interface resulting from galvanic corrosion and strong electrochemical reactions in these regions.

In order to support the above observations and discussion, a local technique based on microcapillaries (EMT) has been employed. EMT studies were conducted after mechanical polishing of the surface of tested specimens. In Fig. 13(a), the local polarization curves ( $1 \text{ mV s}^{-1}$  scan rate) obtained by using EMT (microcapillary was  $50 \text{ }\mu\text{m}$  in diameter, Fig. 1) are presented. LSV has been recorded in the matrix of the ingot—black curve, thixo-cast—blue curve and thixo-cast after T6 HT—magenta curve (Fig. 13b, c and d respectively). It is worth noting that in order to obtain the characteristics of the local corrosion behavior in the matrix of the alloy under different treatment conditions, local LSV curves need to be repeated a few times.

The results revealed differences in the corrosion behavior of the three tested specimens, as can be seen in Fig. 13(a). The

electrochemical response from the matrix of the ingot specimen shows more heterogeneous behavior of the  $\alpha$ -Mg phase in this sample, as confirmed by less reproducible results. Some places have lower current densities, while others have higher values in both the cathodic and anodic ranges. The same observations can be seen when the corrosion potential is considered. There are some sites where corrosion potential is much lower, while others exhibit similar values to those registered for the thixo-cast and thixo-T6 specimens. This indicates nonhomogeneous corrosion behavior, which results from the nonequilibrium state of the ingot's microstructure. In addition, the anodic current densities are higher compared to the thixo-cast and thixo-T6 specimens, which confirms previous observations (see the discussion of EIS results), i.e., more intense anodic (oxidation) reactions in the matrix of the ingot. Thus, it can be concluded that the intensity of the oxidation (corrosion) increases—a thicker corrosion product is formed on the sample surface, which, in turn, causes a higher corrosion resistance in the first period after immersion. (Note that there is no breakdown potential observed in the case of the ingot's matrix contrary to the thixo-cast and thixo-T6 specimens).

In the case of the thixo-cast specimen, first of all the local electrochemical response shows more homogeneous corrosion behavior. The current densities and corrosion potentials registered in the different sites of the matrix are almost the same. The much lower anodic current densities suggest a lower rate of the corrosion processes in the thixomatrix; however, it results in a thinner corrosion product layer. This causes a shorter time of immunity in the first period after immersion.

The courses of the local LSV of the matrix of the thixo-T6 specimen shows similar electrochemical behavior to that observed in the thixo-cast specimen. It is worth noting that the presence of small precipitates enriched in RE in both the

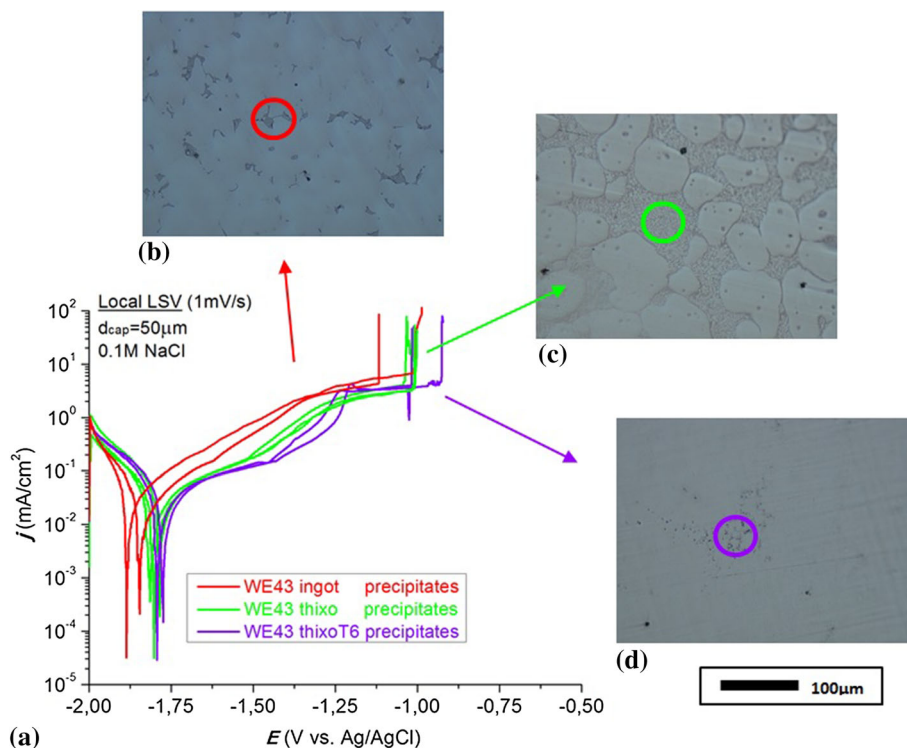


**Fig. 14** (a) Local polarization curves obtained on the precipitates (eutectic) of three tested specimens and optical images showing the measurement locations on: (b) the ingot, (c) thixo-cast, (d) thixo-T6 specimen

thixo and thixo-T6 matrices can be responsible for a higher susceptibility to pitting compared to the ingot's matrix (indicated by the white arrows in Fig. 5 and 6).

Analogically to previous experiments, the local polarization curves recorded for sites with precipitates of intermetallic phases are shown in Fig. 14(a). Higher local electrochemical activity of the ingot specimen can be observed, where lower corrosion potential and higher anodic currents have been registered. The results also indicate heterogeneous corrosion behavior that particularly depends on the size of the precipitate.

In detail, higher corrosion potentials and lower anodic currents are seen in the case of the thixo and thixo-T6 specimens showing their lower local electrochemical activity. Moreover, the measurement values are more homogeneous and present reproducibility. It is worth noting that the breakdown potential is visible in all cases.

It can be concluded that the SSM and SSM/HT processes result in lower electrochemical activity both in the matrix and in sites with precipitates (lower anodic currents).

A simplified model of the corrosion processes is demonstrated in Fig. 15. The magnesium oxide covers the surface of the alloy in the initial state (just before immersion, Fig. 15a). When the specimen comes into contact with the electrolyte, the magnesium hydroxide is formed on the surface according to chemical reaction (1). Simultaneously, the electrochemical reactions (2) and (3) occur (Fig. 15b). Two time constants are observed in the EIS diagrams where the first (in the high frequencies range) is associated with the charge transfer resistance of the  $Mg^{2+}$  ions. Second time constant is attributed to diffusion processes of  $Mg^{2+}$  through the corrosion product of  $Mg(OH)_2$  formed on the surface. The process continues until the  $Mg(OH)_2$  is dissolved somewhere (reaction (4)), and the

corrosion processes start in the weakest regions—usually at sites where the intermetallic phases are present. This has been proved by observations and local LSV (Fig. 11, 12, 13 and 14). Therefore, as the layer of corrosion products becomes thicker, the time needed in order to initiate the corrosion processes increases. The thickness of corrosion products formed on the Mg alloy surface is strongly dependent on microstructure, as was explained above by the experiments and observations.

## 4. Conclusions

The proposed conditions of the SSM process and T6 heat treatment conducted on the WE43 magnesium alloy allowed material to be obtained with improved mechanical parameters and corrosion resistance in a chloride environment (0.1 M NaCl).

The thixoforming procedure (the temperature of 625 °C which corresponds to about 25% of the liquid phase) induced the microstructure changes, where next to the  $\alpha$ -Mg phase as globular grains with the size of  $65.5 \pm 2.1 \mu m$ , a wide eutectic mixture is present in the volume of 26.6 vol.%. The T6 heat treatment of the thixo-cast specimen (saturation from 525 °C/ 5 h/ $H_2O$  and aging of 190 °C/48 h) caused an increase in yield strength to 180 MPa and tensile strength to 280 MPa at the hardness of  $105 \pm 4 HV_5$ .

Both SSM and T6 HT mean that the time for the degradation processes to start in chlorides is slightly shortened compared to the as-cast condition. On the other hand, SSM processing led to changes in the microstructure (a net-shaped eutectic appears) which slows down the degradation processes (inhibiting the



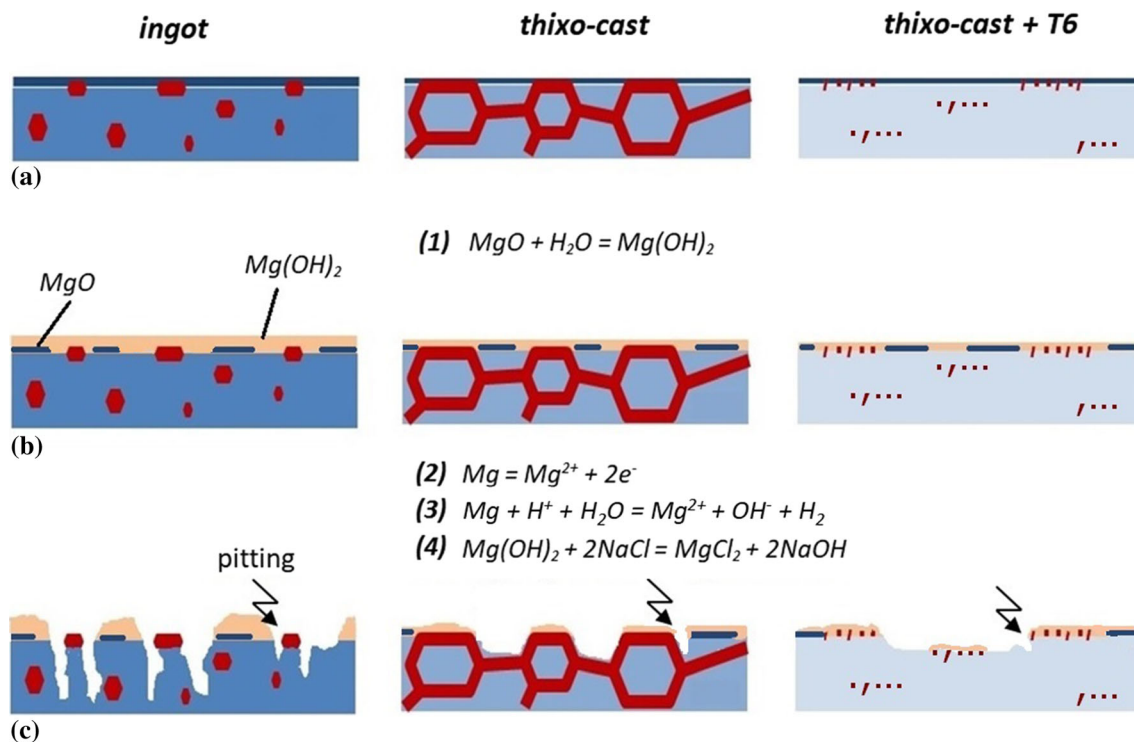


**Fig. 15** Simplified model presenting corrosion processes occurring on the magnesium alloy surface during the immersion test in the 0.1 M NaCl water solution: (a) initial state (just before immersion), (b) after immersion, corrosion products layer is forming; two time constants on EIS are visible, (c) one time constant in EIS is observed (corrosion processes are running—both uniform and pitting corrosion)

corrosion processes that are already running). T6 heat treatment slightly worsens the corrosion resistance of the WE43 magnesium alloy compared with the specimen directly after SSM. The mechanism of the corrosion processes seems to be the same in all three cases; however, the initiation of the corrosion, electrochemical activity and degradation rates are significantly dependent on the microstructure.

## Acknowledgments

The authors gratefully acknowledge the financial support of the Polish National Centre for Research and Development (Grant No.: LIDER/007/151/L-5/13/NCBR/2014).

## Open Access

This article is licensed under a Creative Commons Attribution 4.0 International License, which permits use, sharing, adaptation, distribution and reproduction in any medium or format, as long as you give appropriate credit to the original author(s) and the source, provide a link to the Creative Commons licence, and indicate if changes were made. The images or other third party material in this article are included in the article's Creative Commons licence, unless indicated otherwise in a credit line to the material. If material is not included in the article's Creative Commons licence and your intended use is not permitted by statutory regulation or exceeds the permitted use, you will need to obtain permission directly from the copyright holder. To view a copy of this licence, visit <http://creativecommons.org/licenses/by/4.0/>.

## References

1. ASM Handbook, *Corrosion*, vol. 13 (2003)
2. W.G. Kelvii, A Review of Magnesium/Magnesium Alloys Corrosion and Its Protection, *Recent Patents Corr. Sci.*, 2010, **2**, p 13–21
3. B.L. Mordike and T. Ebert, Magnesium: Properties-Applications-Potential, *Mater. Sci. Eng. A*, 2001, **302**, p 37–45
4. R.W. Cahn, P. Haasen, and E. Kramer, *Materials Science and Technology*, VCH Publishers Inc, New York, 1996
5. E. Ghali, *Corrosion Resistance of Aluminium and Magnesium Alloys—Understanding, Performance and Testing*, Wiley, Hoboken, 2010
6. G.I. Song, Recent Progress in Corrosion and Protection of Magnesium Alloys, *Adv. Eng. Mater.*, 2005, **7**, p 563–586
7. M. Esmaily, J.E. Svensson, S. Fajardo, N. Birbilis, G.S. Frankel, S. Virtanen, R. Arrabal, S. Thomas, and L.G. Johansson, Fundamentals and Advances in Magnesium Alloy Corrosion, *Prog. Mater. Sci.*, 2017, **89**, p 92–193
8. S. Brown, Magnesium: A Structural Super-Metal, *Thoughts and Reflections on the Use of Magnesium*, G. Neighbour and I. Oraifige, Ed., Belmont Press, Northampton, 2017, p 3–5
9. M.M. Avedesian and H. Baker, *ASM Specialty Handbook, Magnesium and Magnesium Alloys*, ASM International, The Mater. Information Society, Ohio, 1999, p 54
10. L.L. Rokhlin, Magnesium Alloys Containing Rare Earth Metals: Structure and Properties, *Advances in Metallic Alloys*, J.N. Fridlyander and G.G. Eskin, Ed., Taylor & Francis, Milton Park, 2003, p 34–68
11. Y.H. Kang, H. Yan, and R.S. Chen, Effects of Heat Treatment on the Precipitates and Mechanical Properties of Sand-Cast Mg-4Y-2.3 Nd-1Gd-0.6 Zr Magnesium Alloy, *Mater. Sci. Eng.*, 2015, **645**, p 361–368
12. S.J. Liu, G.Y. Yang, S.F. Luo, and W.Q. Jie, Microstructure and Mechanical Properties of Sand Mold Cast Mg-4.58 Zn-2.6 Gd-0.18 Zr Magnesium Alloy After different Heat Treatments, *J. Alloys Compd.*, 2015, **644**, p 846–853
13. P. Minarik, R. Kral, and M. Janecek, Effect of ECAP Processing on Corrosion Resistance of AE21 and AE42 Magnesium Alloys, *Appl. Surf. Sci.*, 2013, **281**, p 44–48

14. D.H. StJohn, M.A. Easton, M. Qian, and J.A. Taylor, Grain Refinement of Magnesium Alloys: A Review of Recent Research, Theoretical Developments, and Their Application, *Metall. Mater. Trans. A*, 2013, **44**, p 2935–2949
15. Y. Ali, D. Qiu, B. Jiang, F. Pan, and M. Zhang, Current Research Progress in Grain Refinement of Cast Magnesium Alloys: A Review Article, *J. Alloys Compd.*, 2015, **619**, p 639–651
16. J.W. Chang, X.W. Guo, P.H. Fu, L.M. Peng, and W.J. Ding, Effect of Heat Treatment on Corrosion and Electrochemical Behaviour of Mg-3Nd-0.2 Zn-0.4 Zr (wt.%) alloy, *Electrochim. Acta*, 2007, **52**, p 3160–3167
17. Z. Fan, Semisolid Metal Processing, *Int. Mater. Rev.*, 2002, **47**(2), p 49–85
18. F. Czerwinski, *Magnesium Injection Molding*, Springer, New York, 2008
19. Ł. Rogal, J. Dutkiewicz, A. Góral, B. Olszowska-Sobieraj, and J. Dańko, Characterization of the After Thixoforming Microstructure of a 7075 Aluminium Alloy Gear, *Int. J. Mater. Form.*, 2010, **3**, p 771–774
20. H.V. Atkinson and A. Rassili, *Thixoforming Steel*, Shaker Verlag, Aachen, 2010
21. Z. Zhao, Q. Chen, S. Huang, F. Kang, and Y. Wang, Inhomogeneity of Density and Mechanical Properties of A357 Aluminum Alloy Backward Extruded in Semi-solid State, *Trans. Nonferrous Metals Soc. China*, 2010, **20**(9), p 1630–1637
22. J.A. Valle, M.T. Pérez-Prado, and J.R. Bartolomé, Grain Refinement in a Mg AZ91 Alloy Via Large Strain Hot Rolling, *Mater. Trans.*, 2003, **44**, p 2625–2630
23. Z.S. Ji, M.L. Hu, S. Sugiyama, and J. Yanagimoto, Formation Process of AZ31B Semi-solid Microstructures Through Strain-Induced Melt Activation Method, *Mater. Charact.*, 2008, **59**(7), p 905–911
24. G. Hirt and R. Kopp, *Thixoforming Semi-solid Metal Processing*, Wiley, New York, 2009
25. K.P. Young, C.P. Kyonka, and J.A. Courtois, Fine Grained Metal Composition, US Patent no. 4,415,374, 30 Mar 1982
26. G.L. Song, A. Atrens, X.L. Wu, and B. Zhang, Corrosion behaviour of AZ21, AZ501 and AZ91 in Sodium Chloride, *Corr. Sci.*, 1998, **40**, p 1769–1791
27. R.K. Singh Raman, N. Birbilis, and J. Efthimiadis, Corrosion of Mg Alloy AZ91—The Role of Microstructure, *Corr. Eng. Sci. Technol.*, 2004, **39**, p 346–350
28. O. Lunder, J.E. Lein, T.K. Aune, and K. Nisancioglu, The Role of Mg17Al12 Phase in the Corrosion of Mg Alloy AZ91, *Corrosion*, 1989, **45**, p 741–748
29. J.H. Nordlien, K. Nisancioglu, S. Ono, and N. Masuko, Morphology and Structure of Water-Formed Oxides on Ternary MgAl Alloys, *J. Electrochem. Soc.*, 1997, **144**, p 461–466
30. G. Song and A. Atrens, Understanding Magnesium Corrosion—A Framework for Improved Alloy Performance, *Adv. Eng. Mater.*, 2003, **5**, p 837–858
31. M. Anik and G. Celikten, Analysis of the Electrochemical Reaction Behavior of Alloy AZ91 by EIS Technique in H<sub>3</sub>PO<sub>4</sub>/KOH Buffered K<sub>2</sub>SO<sub>4</sub> Solutions, *Corr. Sci.*, 2007, **49**, p 1878–1894
32. G.L. Song, A. Atrens, and M. Dargusch, Influence of Microstructure on the Corrosion of Diecast AZ91D, *Corr. Sci.*, 1999, **41**, p 249–273
33. G.L. Song, A.L. Bowles, and D.H. StJohn, Corrosion Resistance of Aged Die Cast Magnesium Alloy AZ91D, *Mater. Sci. Eng.*, 2004, **366**, p 74–86
34. T. Zhang, Y. Li, and F.H. Wang, Roles of  $\beta$  Phase in the Corrosion Process of AZ91D Magnesium Alloy, *Corr. Sci.*, 2006, **48**, p 1249–1264
35. R. Ambat, N.N. Aung, and W. Zhou, Evaluation of Microstructural Effects on Corrosion Behaviour of AZ91D Magnesium Alloy, *Corr. Sci.*, 2000, **42**, p 1433–1455
36. M. Anik, P. Avci, A. Tanverdi, I. Celikyurek, B. Baksan, and B. Gurler, Effect of the Eutectic Phase Mixture on the Anodic Behavior of Alloy AZ91, *Mater. Des.*, 2006, **27**, p 347–355
37. G. Ballerini, U. Bardi, R. Bignucolo, and G. Ceraolo, About Some Corrosion Mechanisms of AZ91D Magnesium Alloy, *Corr. Sci.*, 2005, **47**, p 2173–2184
38. W.C. Neil, M. Forsyth, P.C. Howlett, C.R. Hutchinson, and B.R.W. Hinton, Corrosion of Magnesium Alloy ZE41—The Role of Microstructural Features, *Corr. Sci.*, 2009, **51**, p 387–394
39. H. Krawiec, S. Stanek, V. Vignal, J. Lelito, and J.S. Suchy, The Use of Microcapillary Techniques to Study the Corrosion Resistance of AZ91 Magnesium Alloy at the Microscale, *Corr. Sci.*, 2011, **53**, p 3108–3113
40. E. Koç, M.B. Kannan, M. Ünal, and E. Candan, Influence of Zinc on the Microstructure, Mechanical Properties and in Vitro Corrosion Behavior of Magnesium-Zinc Binary Alloys, *J. Alloys Compd.*, 2015, **648**, p 291–296
41. Properties and Selection: *Nonferrous alloys and Special Purpose Materials—Selection and Application of Magnesium and Magnesium Alloys*, ASM Handbook, vol 2
42. A.P.M. Saad and A. Syahrom, Study of Dynamic Degradation Behaviour of Porous Magnesium Under Physiological Environment of Human Cancellous Bone, *Corr. Sci.*, 2018, **131**, p 45–56
43. Y.F. Zheng, X.N. Gu, and F. Witte, Biodegradable Metals, *Mater. Sci. Eng. R*, 2014, **77**, p 1–34
44. M.I. Jamesh, G. Wu, Y. Zhao, D.R. McKenzie, M.M.M. Bilek, and P.K. Chu, Electrochemical Corrosion Behavior of Biodegradable Mg-Y-RE and Mg-Zn-Zr Alloys in Ringer's Solution and Simulated Body Fluid, *Corr. Sci.*, 2015, **91**, p 160–184
45. M. Ascencio, M. Pekguleryuz, and S. Omanovic, An Investigation of the Corrosion Mechanisms of WE43 Mg Alloy in a Modified Simulated Body Fluid Solution: the Influence of Immersion Time, *Corr. Sci.*, 2014, **87**, p 489–503
46. Y. Liu, S. Zheng, N. Li, H. Guo, Y. Zheng, and J. Peng, Study on the in Vitro Degradation Behavior of Pure Mg and WE43 in Human Bile for 60 Days for Future Usage in Biliary, *Mater. Lett.*, 2016, **179**, p 100–103
47. Ł. Rogal and G. Garzel, Semi-solid State Mixing of Mg-Zn-RE Alloys—Microstructure and Mechanical Properties, *J. Mater. Process. Technol.*, 2019, **264**, p 352–365
48. N. Perez, *Electrochemistry and Corrosion Science*, Kluwer, Boston, 2004
49. P.A. Schweitzer, *Fundamentals of Corrosion—Mechanisms, Causes and Preventative Methods*, CRC Press, Boca Raton, 2009
50. H. Böhni, T. Suter, and A. Schreyer, Micro- and Nanotechniques to Study Localized Corrosion, *Electrochimica Acta*, 1995, **40**, p 1361–1368
51. T. Suter and H. Böhni, Microelectrodes for Studies of Localized Corrosion Processes, *Electrochimica Acta*, 1998, **43**, p 2843–2849
52. T. Suter and H. Böhni, A New Microelectrochemical Method to Study Pit Initiation on Stainless Steels, *Electrochimica Acta*, 1997, **42**, p 3275–3280
53. H. Krawiec and Z. Szklarz, Combining the Electrochemical Microcell Technique and the Electron Backscatter Diffraction Method to Study the Electrochemical Behaviour of Polycrystalline Aluminium in Sodium Chloride Solution, *Electrochimica Acta*, 2016, **203**, p 426–438
54. H. Krawiec, Z. Szklarz, and V. Vignal, Influence of Applied Strain on the Microstructural Corrosion of AlMg<sub>2</sub> As-Cast Aluminium Alloy in Sodium Chloride Solution, *Corr. Sci.*, 2012, **65**, p 387–396
55. M. Slezak, P. Bobrowski, and Ł. Rogal, Microstructure Analysis and Rheological Behavior of Magnesium Alloys at Semi-solid Temperature Range, *J. Mater. Eng. Perform.*, 2018, **27**(9), p 4593–4605
56. D. Qiu and M.-X. Zhang, Effect of Active Heterogeneous Nucleation Particles on the Grain Refining Efficiency in an Mg-10 wt% Y Cast Alloy, *J. Alloys Compd.*, 2009, **488**(1), p 260–264
57. T.B. Massalski, H. Okamoto, P.R. Subramanian, and L. Kacprzak, *Binary Alloy Phase Diagrams-Second edition*, ASM International, Materials Park, 1990
58. D. Qiu and M.X. Zhan, Effect of Active Heterogeneous Nucleation Particles on the Grain Refining Efficiency in an Mg-10wt.%Y Cast Alloy, *J. Alloys Compd.*, 2009, **488**, p 260–264
59. D.H. Kirkwood, Semisolid Metal Processing, *Int. Mater. Rev.*, 1994, **39**, p 173–189
60. Ł. Rogal and J. Dutkiewicz, Globular Microstructure Formation in X210CrW12 Steel for Semi-solid Processing Using Plastic Deformation or Boron Modification, *Arch. Metall. Mater.*, 2012, **58**, p 751–755
61. Ł. Rogal, F. Czerwinski, L. Litwinska-Dobrzyńska, P. Bobrowski, A. Wierzbica-Miernik, and J. Dutkiewicz, Effect of hot Rolling and Equal-Channel Angular Pressing on Generation of Globular Microstructure in Semi-solid Mg-3% Zn alloy, *Solid State Phenomena*, 2014, **217**, p 381–388

62. J. Polmear, *Light Alloys*, M.A. Burlington, Ed., Elsevier/Butterworth-Heinemann, Oxford, 2006,
63. J. Polmear, Magnesium Alloys and Applications, *Mater. Sci. Technol.*, 1994, **10**, p 1–16
64. K. Maruyama, M. Suzuki, and H. Sato, Creep Strength of Magnesium-Based Alloys, *Metall. Mater. Trans. A.*, 2002, **33**, p 875–882
65. G.L. Song and A. Atrens, Corrosion Mechanisms of Magnesium Alloys, *Adv. Eng. Mater.*, 1999, **1**, p 1
66. N. Pebere, C. Riera, and F. Dabosi, Investigation of Magnesium Corrosion in Aerated Sodium Sulfate Solution by Electrochemical Impedance Spectroscopy, *Electrochim. Acta*, 1990, **35**, p 555–561
67. C. Cao, On the Impedance Plane Displays for Irreversible Electrode Reactions Based on the Stability Conditions of the Steady-State—I. One State Variable Besides Electrode Potential, *Electrochim. Acta*, 1990, **35**, p 837–844
68. G. Baril, Ch Blanc, and N. Pebere, AC Impedance Spectroscopy in Characterizing Time-Dependent Corrosion of AZ91 and AM50 Magnesium Alloys Characterization with Respect to Their Microstructures, *J. Electrochem. Soc.*, 2001, **148**(12), p B489–B496
69. H. Krawiec, V. Vignal, and Z. Szklarz, Local Electrochemical Studies of the Microstructural Corrosion of AlCu4Mg1 As-Cast Aluminium Alloy and Influence of Applied Strain, *J. Solid State Electrochem.*, 2009, **13**, p 1181–1191
70. F. Cao, G.-L. Song, and A. Atrens, Corrosion and Passivation of Magnesium Alloys, *Corr. Sci.*, 2016, **111**, p 835–845

**Publisher's Note** Springer Nature remains neutral with regard to jurisdictional claims in published maps and institutional affiliations.